



## Long-wavelength character of subducted slabs in the lower mantle

Marie Běhounková<sup>a,b,\*</sup>, Hana Čížková<sup>a</sup>

<sup>a</sup> Charles University in Prague, Faculty of Mathematics and Physics, Department of Geophysics, V Holešovičkách 2, 180 00 Praha 8, Czech Republic

<sup>b</sup> Geophysical Institute of the Academy of Sciences, Boční II/1401, 141 31 Praha 4, Czech Republic

### ARTICLE INFO

#### Article history:

Received 19 January 2008

Received in revised form 31 July 2008

Accepted 31 July 2008

Available online 19 September 2008

Editor: R.D. van der Hilst

#### Keywords:

subduction process

slab thickening

non-linear rheology

tomography

### ABSTRACT

The high resolution seismic tomography provides the detailed information about the fate of the subducted plates in the mantle. While the slab deformation in the transition zone is quite complex and differs among the individual subduction zones, it could be generally concluded that most slabs seem to penetrate into the lower mantle. The character of the fast seismic velocity anomalies, however, changes when the slabs cross the 670 km discontinuity. While in the upper mantle tomography resolves relatively narrow plate-like structures, in the lower mantle it rather indicates thick blobs of seismically fast material. Such thickening of the downgoing slabs is traditionally attributed to the effect of the viscosity increase in the lower mantle. Here we study the deformation of the slabs in the lower mantle in a viscous model with a non-linear composite rheology including the diffusion creep, the dislocation creep and a power-law stress limiter. We perform numerical simulations of the subduction process in a 2D Cartesian domain and concentrate especially on the effect of the change of the rheological parameters across the 670 km boundary on the slab deformation in the upper part of the lower mantle. The thickening or the buckling of the plate is indeed observed in the models with relatively low yield stress (0.1 GPa) of the stress-limiting mechanism and with a viscosity increase at the 670 km discontinuity. Further, we show that both the major mantle phase transitions and the strength of the crust layer have significant consequences for the creation of the buckling instabilities in the lower mantle.

© 2008 Elsevier B.V. All rights reserved.

### 1. Introduction

Recent seismic tomographic models mapping the subduction areas in detail provide unique information about the structure of the subducted plates. Interpretation of these heterogeneities is an important issue. From high resolution tomographic models (e.g. Bijwaard et al., 1998; Kárason and van der Hilst, 2001), fast seismic anomalies traditionally connected to the subducting plates seem to be significantly thickened after they penetrate into the lower mantle.

Further, the plate-like character of the downwelling anomalies seems to vanish and the blob-like features are observed in the lower mantle. This thickening might be attributed to the lack of the resolution of the tomographic inversion—the thin slabs could be mapped as thick anomalies due to the smearing effects of the inversion technique. The resolution of the tomographic models is, however, widely tested using the resolution matrix (e.g. Vasco et al., 2003) or the standard resolution tests (e.g. Inoue et al., 1990; Su et al., 1994; Vasco et al., 1995; Kárason and van der Hilst, 2001; Fukao et al., 2003; Ren et al., 2007). Special attention has been paid to the

subduction zones (e.g. van der Hilst, 1995; van der Hilst et al., 1997; Bijwaard et al., 1998), where the detailed tests were performed to determine the resolution of the structure of the slabs. The tomographers conclude that their models are able to resolve the slab structure—the penetration into the lower mantle and the broadening of the slab in the top of the lower mantle.

The slab thickening in the lower mantle in the regions such as Tonga, Marianas and Kuril has been addressed by several authors (e.g. Giardini and Woodhouse, 1984; Creager and Jordan, 1986; Fischer and Jordan, 1991; Boyd and Creager, 1991; van der Hilst, 1995). Ribe et al. (2007) mention that the width of the slabs may thicken from 50–100 km above the 670 km boundary up to more than 400 km below it in Central America and Java zones.

They also suggest apparent thickening by factors of up to five in the Marianas, Kuril-Kamchatka and Tonga. Such an increase of the wavelengths of the cold downwellings may also be required by the geodynamical interpretations of the long-wavelength geoid (Ricard et al., 1993) or long-term variations of the Earth's moment of inertia (Richards et al., 1997).

To be able to explain the slab long-wavelength character (thickening or blobbing of the slabs) in the lower mantle, the subducting plate has to pass through some mechanical barrier. At the depth of 670 km, the subducting plate is passing through the endothermic phase transition which forms a barrier against the slab penetration into the lower mantle (e.g. Christensen and Yuen, 1984; Tackley et al., 1993). In the lower mantle, a significant increase of the viscosity is also

\* Corresponding author. Present address: Laboratoire de Planétologie et Géodynamique, UMR 6112, CNRS-Université de Nantes, Nantes, France.

E-mail addresses: [behounek@karel.troja.mff.cuni.cz](mailto:behounek@karel.troja.mff.cuni.cz), [marie.behounkova@gmail.com](mailto:marie.behounkova@gmail.com) (M. Běhounková).

expected. The increase by a factor 10–100 (e.g. Hager and Richards, 1989; Peltier, 1996; Lambeck and Johnston, 1998) or even 1000 (Kido and Čadek, 1997) is predicted. Possible mechanisms of the thickening of the slabs are compression due to the increasing viscous resistance with depth (e.g. Bunge et al., 1996; Čížková and Čadek, 1997) or the fluid buckling (Griffiths and Turner, 1988; Guillou-Frottier et al., 1995; Griffiths et al., 1995; Ribe, 2003). The compression is, however, supposed to thicken the slab approximately twice (Gurnis and Hager, 1988; Gaherty and Hager, 1994); therefore it may not be able to explain the tomographic results. The buckling, on the other hand, is able to explain even larger thickening (Ribe et al., 2007).

We employ the forward modeling method to study the circumstances under which the thickening of the subducting slabs occurs in the lower mantle. The deformation and potential thickening of the subducting plate in the lower mantle depends on several parameters, especially, on the rheological properties. The rheology of the mantle material is known to be non-linear but its parameters are rather uncertain especially in the lower mantle. We use here a viscous model with the composite rheology including diffusion creep, dislocation creep and a power-law stress limiter approximating Peierl's creep.

We study the influence of the yield stress, viscosity increase at 670 km depth and the crustal strength on the slab deformation and potential thickening or buckling in the upper part of the lower mantle. Further, we also look at the effects of major mantle phase transitions and the surface boundary condition.

## 2. Model

The thermo-chemical convection in the Earth's mantle is described by the equations based on conservation laws, rheology description, the equation of state and the material advective transport equation. We use the incompressible extended Boussinesq approximation with infinite Prandtl number (Ito and King, 1994). Therefore, the density is assumed to be constant except for the buoyancy term and the inertia is neglected. Moreover, the velocity field is divergence-free (incompressible flow). Further, we neglect self-gravitation.

Inside the model domain excluding boundaries, we use the following dimensionless equations (used symbols are given in Table 1):

$$\partial_j v_j = 0, \quad (1)$$

$$-\partial_i \pi + \partial_j \sigma_{ij} = \left( Ra(T - T_{ref}) - \sum_k Rb_k \Gamma_k - Rcc \right) \frac{g_i}{g_0}, \quad (2)$$

$$\frac{DC}{Dt} = 0, \quad (3)$$

$$\frac{\partial T}{\partial t} = \partial_j \partial_j T - v_j \partial_j T + Di \left( T + \frac{T_S}{T_B - T_S} \right) \frac{g_i v_j}{g_0} + \frac{Di}{Ra} \sigma_{ij} \partial_j u_i + \sum_k \frac{Rb_k}{Ra} Di \left( T + \frac{T_S}{T_B - T_S} \right) \gamma_k^i \frac{D\Gamma_k^i}{Dt}, \quad (4)$$

where  $\frac{D}{Dt}$  is a material time derivative and  $\gamma_k^i$  is dimensionless Clapeyron slope ( $\gamma_k^i = \gamma_k^i \frac{T_B - T_S}{\rho_0 g_0 d}$ ). They describe mass conservation (Eq. (1)), momentum conservation (Eq. (2)) and compositional changes due to the compositional advection (Eq. (3)). The temperature changes in the time are given by Eq. (4)—they are caused by heat diffusion, heat advection, adiabatic heating/cooling, shear heating and latent heat release or consumption. We use the code CBMIC (Běhounková, 2007) based on the method proposed by Gerya and Yuen (2003), to solve the system ((1)–(4)) in a 2D Cartesian domain. Eqs. (1)–(2) and the heat Eq. (4) without advection and latent heating are solved using the finite differences on the staggered grid. The advection and latent heating parts of the heat equation (Eq. (4)) and the material advection (Eq. (3)) are solved using marker technique (e.g. Christensen and Yuen, 1984; Hockney and Eastwood, 1988; Gerya et al., 2000). Our models include

**Table 1**

Used symbols and parameters

ith component of the velocity	$u_i$
ijth component of the stress tensor $-\pi\delta_{ij} + \sigma_{ij}$	$\tau_{ij}$
Dynamic pressure	$\pi$
ijth component of the deviatoric part of the stress tensor	$\sigma_{ij}$
Temperature	$T$
Reference temperature (geotherm)	$T_{ref}$
Time	$t$
Phase function for the kth phase transition	$\Gamma_k$
Composition parameter	$C$
Rayleigh number $\frac{\rho_0 \alpha_0 (T_B - T_S) d^3}{\eta_0 \kappa_0}$	$Ra$ $2 \cdot 10^7$
Phase Rayleigh number $\frac{\rho_0 \alpha_0 \gamma_k^i d^3}{\eta_0 \kappa_0}$	$Rb_k$
Compositional Rayleigh number $\frac{\rho_0 c_0 d^3}{\eta_0 \kappa_0}$	$Rc$ 0
Gravity acceleration	$g_0$ $10 \text{ m} \cdot \text{s}^{-2}$
Height of the model domain	$d$ 2000 km
Surface temperature	$T_S$ 273 K
Bottom temperature	$T_B$ 2753 K
Potential temperature	$T_{pot}$ 1573 K
Reference density	$\rho_0$ $3400 \text{ kg} \cdot \text{m}^{-3}$
Reference thermal conductivity	$k_0$ $5 \text{ W} \cdot \text{m}^{-1} \cdot \text{K}^{-1}$
Reference thermal diffusivity $\frac{k_0}{\rho_0 c_p}$	$\kappa_0$ $1.18 \cdot 10^{-6} \text{ m}^2 \cdot \text{s}^{-1}$
Heat capacity	$c_p$ $1250 \text{ J} \cdot \text{kg}^{-1} \cdot \text{K}^{-1}$
Reference thermal expansivity	$\alpha_0$ $3.5 \cdot 10^{-5} \text{ K}^{-1}$
Prescribed plate velocity for models with kinematic condition	$v_x$ $5 \text{ cm} \cdot \text{yr}^{-1}$
Phase transition at 400 km	
Clapeyron slope <sup>a</sup>	$\gamma_{400}$ $3.0 \text{ MPa} \cdot \text{K}^{-1}$
Density difference <sup>b</sup>	$\delta\rho_{400}$ $273 \text{ kg} \cdot \text{m}^{-3}$
Phase transition at 670 km	
Clapeyron slope <sup>a</sup>	$\gamma_{670}$ $-2.5 \text{ MPa} \cdot \text{K}^{-1}$
Density difference <sup>b</sup>	$\delta\rho_{670}$ $342 \text{ kg} \cdot \text{m}^{-3}$
Width of all phase transitions	$d_{ph}$ 5 km
Molar gas constant	$R$ $8.3143 \text{ J} \cdot \text{K}^{-1} \cdot \text{mol}^{-1}$
Maximum viscosity	$\eta_{max}$ $10^{28} \text{ Pa} \cdot \text{s}$
Reference viscosity	$\eta_0$ $10^{21} \text{ Pa} \cdot \text{s}$
Yield stress	$\sigma_y$ $10^8, 10^9 \text{ Pa}$
Reference strain rate in yield strength determination	$\dot{\epsilon}_y$ $10^{-15} \text{ s}^{-1}$
Yield stress exponent	$n_y$ 5
Viscosity of decoupling layer	$\eta_{DL}$ $10^{19}, 10^{21} \text{ Pa} \cdot \text{s}$
Pre-factor coefficient in the upper mantle	$C_{UM}$ 1
Pre-factor coefficient in the lower mantle	$C_{LM}$ 1, 10, 30
Upper mantle parameters: <sup>c</sup>	
Pre-exponential parameter of diffusion creep	$A_{diff}^*$ $1.92 \cdot 10^{-10} \text{ Pa}^{-1} \cdot \text{s}^{-1}$
Activation energy for diffusion creep	$E_{diff}^*$ $300 \cdot 10^3 \text{ J} \cdot \text{mol}^{-1}$
Activation volume for diffusion creep	$V_{diff}^*$ $6.0 \cdot 10^{-6} \text{ m}^3 \cdot \text{mol}^{-1}$
Pre-exponential parameter of dislocation creep	$A_{disl}^*$ $2.42 \cdot 10^{-16} \text{ Pa}^{-n} \cdot \text{s}^{-1}$
Activation energy for dislocation creep	$E_{disl}^*$ $540 \cdot 10^3 \text{ J} \cdot \text{mol}^{-1}$
Activation volume for dislocation creep	$V_{disl}^*$ $15 \cdot 10^{-6} \text{ m}^3 \cdot \text{mol}^{-1}$
Power-law stress exponent	$n$ 3.5
Lower mantle parameters: <sup>d</sup>	
Pre-exponential parameter of diffusion creep	$A_{diff}^*$ $3.65 \cdot 10^{-15} \text{ Pa}^{-1} \cdot \text{s}^{-1}$
Activation energy for diffusion creep	$E_{diff}^*$ $208 \cdot 10^3 \text{ J} \cdot \text{mol}^{-1}$
Activation volume for diffusion creep	$V_{diff}^*$ $2.5 \cdot 10^{-6} \text{ m}^3 \cdot \text{mol}^{-1}$
Pre-exponential parameter of dislocation creep	$A_{disl}^*$ $6.63 \cdot 10^{-32} \text{ Pa}^{-n} \cdot \text{s}^{-1}$
Activation energy for dislocation creep	$E_{disl}^*$ $285 \cdot 10^3 \text{ J} \cdot \text{mol}^{-1}$
Activation volume for dislocation creep	$V_{disl}^*$ $1.37 \cdot 10^{-6} \text{ m}^3 \cdot \text{mol}^{-1}$
Power-law stress exponent	$n$ 3.5

<sup>a</sup> Bina and Helffrich (1994).

<sup>b</sup> Steinbach and Yuen (1995).

<sup>c</sup> Adapted from Karato and Wu (1993).

<sup>d</sup> Yamazaki and Karato (2001), Frost and Ashby (1982), see text for details.

the exothermic phase transition at 400 km and the endothermic phase transition at 670 km.

For the description of the phase transitions effect, we use the phase function  $\Gamma_k$  (Christensen and Yuen, 1985) with the harmonic parametrization (van Hunen, 2001)

$$\Gamma_k = \begin{cases} 0 & z < z_{ph} - 1/2d_{ph} \\ \frac{1}{2} \left( 1 + \sin \left( 2\pi \frac{z - z_{ph}^k(T)}{d_{ph}^k} \right) \right) & z_{ph} - 1/2d_{ph} < z < z_{ph} + 1/2d_{ph} \\ 1 & z > z_{ph} + 1/2d_{ph} \end{cases} \quad (5)$$

The phase function parameter  $\Gamma_k$  varies between 0 and 1 and gives the proportion of the  $k$ th phase,  $d_{ph}^k$  is a parameter defining the transition width,  $z$  is the depth and  $z_{ph}^k$  is the depth of the  $k$ th phase transition. For the detailed method and code description see Běhounková (2007).

The model setup is illustrated in Fig. 1a. The model is 7000 km wide and 2000 km deep. A ridge is positioned in the left-hand side upper corner. Plate width increases from the ridge to the trench following the half-space cooling model reaching the maximal age 100 My at the trench. The subducting plate is 5000 km long. The over-riding plate is positioned to the right from the trench ( $x > 5000$  km) and its width corresponds to the 100 My old plate at the beginning of the simulation. On the top of the subducting plate, there is a 10 km thick layer of relatively weak material. This crust-like layer enables the separation of the subducting and over-riding plates. Its characteristics are, however, rather simple (constant viscosity and no compositional density contrast) compared to complex properties of the real crust. The geometry of this decoupling layer on the contact between the subducting and the over-riding plates is given in Fig. 1b. For numerical convenience, the rheological properties of the decoupling layer are replaced by the rheological properties of the mantle material at the depth of 200 km. Beneath the plate, the initial temperature distribution follows an adiabatic profile with potential temperature  $T_{pot} = 1573$  K

$$T_{adiab}(z) = T_{pot} \exp\left(\frac{\alpha_0 g_0 z}{c_p}\right) \quad (6)$$

The vertical temperature profile taken at the trench ( $x = 5000$  km) is shown in Fig. 1c. Since the choice of the velocity boundary conditions especially on the top boundary of the model domain may influence the stress field within the slabs (e.g. Čížková et al., 2007) we test here both dynamic (free-slip, impermeable) and kinematic (prescribed velocity) boundary conditions at the surface. In the models with the kinematic boundary conditions, the horizontal velocity prescribed at the subducting plate is  $v_x = 5$  cm·yr<sup>-1</sup> while no-slip is required at the over-riding plate. The impermeable free-slip

boundary conditions are used on the left-hand side, right-hand side and bottom boundaries. The boundary conditions for the heat Eq. (4) are as follows: on the top boundary the surface temperature  $T_S$  (Table 1) is prescribed except for the left-hand side upper corner nodal point, where the potential temperature  $T_{pot}$  is specified (the higher temperature ensures the lower viscosity at the ridge). On the bottom boundary, the temperature is  $T_B$ . On the left- and right-hand side boundaries, zero heat flux is prescribed. The values of all used parameters are in Table 1.

In the models with the free-slip condition at the top boundary, the ridge push in the initial setup (Fig. 1a) is not strong enough to overcome the friction at the contact of the plates and the resistance against the bending and the subduction process does not start on its own. That is why we first run a short calculation with the prescribed velocity on the top of the subducting plate in order to develop a slab tip subducted to the depth of about 200 km. Then the slab pull is already strong enough to maintain the subduction process, the kinematic boundary condition is switched off and the calculation is carried on with the free-slip boundary condition (Čížková et al., 2007).

The resolution of the Eulerian grid on the left-hand side is ~40 km, and the grid shrinks in the horizontal direction (the distance between the nodes of the Eulerian grid decreases with the coefficient  $c = 1.03$ ). Maximum resolution 3.33 km is reached for  $x \in (4800-5300)$  km. Then the grid expands with coefficient  $c = 1.035$  and the minimum resolution on the right-hand side is ~50 km. In the vertical direction, the maximum resolution is 3 km for  $z < 90$  km.

The resolution down to  $z = 700$  km is 10 km, and the resolution near bottom of the model is ~60 km. The expansion of the grid is limited by factors 1.03 and 1.04. In each cell, we have 100 temperature markers and 150 chemical markers at the beginning.

The mantle material is treated as a viscous fluid

$$\sigma_{ij} = \eta(\partial_j v_i + \partial_i v_j). \quad (7)$$

We use a composite model (van den Berg et al., 1993) including diffusion creep, dislocation creep and a power-law stress limiter

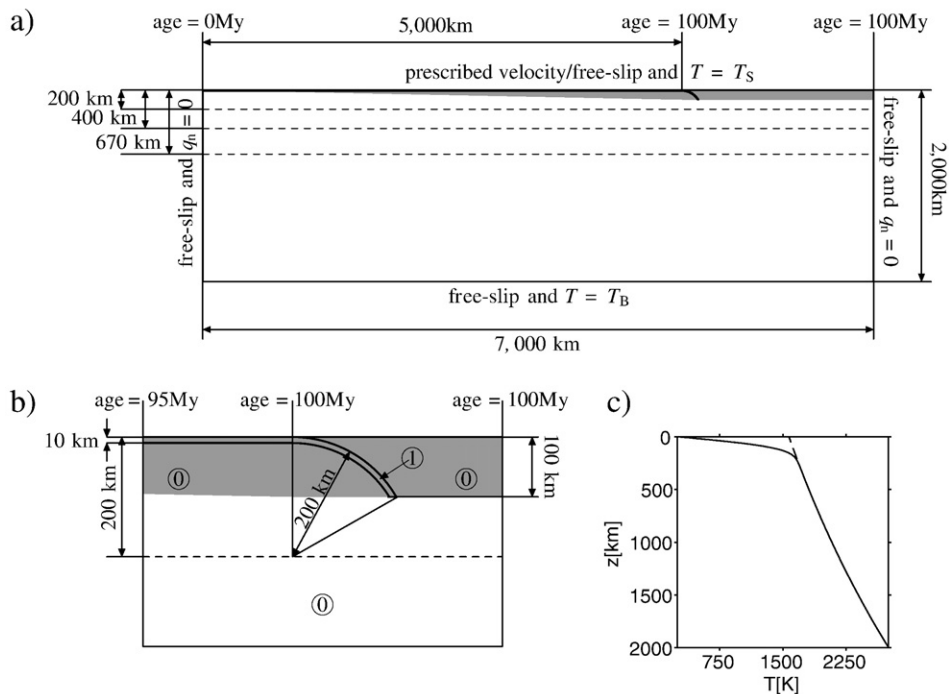


Fig. 1. Initial and boundary conditions; a) setup of the whole model domain, b) detail of the trench area—initial distribution of the mantle material (0) and the decoupling crust material (1), c) vertical profile of the initial temperature for the 100 My old plate (solid line) and an adiabatic profile for potential temperature  $T_{pot} = 1573$  K (dashed line).

approximating the strongly non-linear Peierl's creep (van Hunen et al., 2004). Effective viscosity is expressed as follows:

$$\eta_{\text{eff}} = \left( \frac{1}{\eta_{\text{diff}}} + \frac{1}{\eta_{\text{disl}}} + \frac{1}{\eta_y} + \frac{1}{\eta_{\text{max}}} \right)^{-1}, \quad (8)$$

where  $\eta_{\text{diff}}$ ,  $\eta_{\text{disl}}$  and  $\eta_y$  are the viscosities of the diffusion creep, dislocation creep, and the stress-limiting mechanism respectively.  $\eta_{\text{max}}$  is a maximum viscosity introduced to limit the effective viscosity in the coldest shallow parts of the model and do not dominate in the vicinity of the plates' contact. Pressure and temperature dependence of the viscosities of the diffusion creep and the dislocation creep follows Arrhenius' law

$$\eta_{\text{diff}} = CA_{\text{diff}}^{-1} \exp\left(\frac{E_{\text{diff}}^* + pV_{\text{diff}}^*}{RT}\right), \quad (9)$$

$$\eta_{\text{disl}} = CA_{\text{disl}}^{-1/n} \dot{\epsilon}_{\text{II}}^{(1-n)/n} \exp\left(\frac{E_{\text{disl}}^* + pV_{\text{disl}}^*}{nRT}\right). \quad (10)$$

Stress limiter viscosity  $\eta_y$  is calculated using (van Hunen et al., 2004)

$$\eta_y = C\sigma_y \dot{\epsilon}_y^{-1/n_y} \dot{\epsilon}_{\text{II}}^{1/n_y-1}. \quad (11)$$

The power-law index  $n_y$  defines the brittleness of the material. For  $n_y=1$  the viscosity is kept constant, independent on the strain rate or stress while for  $n_y$  going to infinity we define a maximum stress regardless of the strain rate. Here we apply the value  $n_y=5$  and the stress limiter behaves like a power-law creep mechanism. The stress limiter replaces effectively Peierl's mechanism—low temperature plasticity (Kameyama et al., 1999). And two values of the yield stress  $-\sigma_y=0.1$  GPa or  $\sigma_y=1$  GPa are taken into account in our models.

In addition to the pre-exponential parameters  $A_{\text{diff}}$  and  $A_{\text{disl}}$ , we introduce another factor  $C$  which defines the viscosity jump over the 670 km boundary.  $C_{\text{UM}}=1$  in the upper mantle, while in the lower mantle  $C_{\text{LM}}$  has the value 1, 10 or 30. Further, two values of the viscosity of the decoupling layer,  $10^{19}$  or  $10^{21}$  Pa·s, are tested. The rheological parameters such as the activation energy  $E^*$ , activation volume  $V^*$ , pre-exponential parameters  $A$  and viscosity stress-exponent  $n$  are listed in Table 1. We use different parameters for the upper and the lower mantle materials. For the upper mantle (UM), the parameters are adapted from Karato and Wu (1993). In the lower mantle (LM), the rheological parameters are less constrained. Here we use parameters based on Yamazaki and Karato (2001) and Frost and Ashby (1982). They both use viscosity parametrization based on homologous temperature. We estimate our activation parameters by fitting their viscosity curves. In order to control the viscosity increase just by the parameter  $C$ , our lower mantle pre-exponential parameters  $A_{\text{diff}}^{\text{LM}}$  and  $A_{\text{disl}}^{\text{LM}}$  are computed from the conditions  $\eta_{\text{diff}}^{\text{UM}}(670 \text{ km}) = \eta_{\text{diff}}^{\text{LM}}(670 \text{ km})$  and  $\eta_{\text{disl}}^{\text{UM}}(670 \text{ km}) = \eta_{\text{disl}}^{\text{LM}}(670 \text{ km})$ , thus ensuring the continuous viscosities across the 670 km boundary if the additional viscosity jump is not included and the factor  $C$  is the same in the upper and lower mantle. The viscosity jump at 670 km is then controlled solely by the upper and lower mantle value of the factor  $C$  and it is a free parameter of the models.

### 3. Results

We will discuss now the results of several model runs with various values of viscosity increase in the lower mantle, the strength of the decoupling layer, the stress limit and the surface boundary conditions. The list of models is given in Table 2. The last column of Table 2 gives the detailed description of the boundary condition—for how long the kinematic boundary condition was run before the free-slip was switched on. Only in the model with the low stress limit and weak decoupling layer (models Tsy8d19), the slab starts to subduct on its

**Table 2**

List of the models and their parameters

Model	$\sigma_y$ [GPa]	$\eta_{\text{DL}}$ [Pa·s]	C	boundary condition
Tsy8d19C01_v	0.1	$10^{19}$	1	prescribed velocity
Tsy8d19C10_v	0.1	$10^{19}$	10	prescribed velocity
Tsy8d19C30_v	0.1	$10^{19}$	30	prescribed velocity
Tsy8d19C01_fs00	0.1	$10^{19}$	1	free-slip from the beginning of the simulation
Tsy8d19C10_fs00	0.1	$10^{19}$	10	free-slip from the beginning of the simulation
Tsy8d19C30_fs00	0.1	$10^{19}$	30	free-slip from the beginning of the simulation
Tsy8d21C01_v	0.1	$10^{21}$	1	prescribed velocity
Tsy8d21C10_v	0.1	$10^{21}$	10	prescribed velocity
Tsy8d21C30_v	0.1	$10^{21}$	30	prescribed velocity
Tsy8d21C01 fs10	0.1	$10^{21}$	1	prescribed velocity ( $t < 10$ My), free-slip ( $t > 10$ My)
Tsy8d21C10 fs10	0.1	$10^{21}$	10	prescribed velocity ( $t < 10$ My), free-slip ( $t > 10$ My)
Tsy8d21C30 fs10	0.1	$10^{21}$	30	prescribed velocity ( $t < 10$ My), free-slip ( $t > 10$ My)
Tsy9d19C01_v	1.0	$10^{19}$	1	prescribed velocity
Tsy9d19C10_v	1.0	$10^{19}$	10	prescribed velocity
Tsy9d19C30_v	1.0	$10^{19}$	30	prescribed velocity
Tsy9d19C01_fs08	1.0	$10^{19}$	1	prescribed velocity ( $t < 8$ My), free-slip ( $t > 8$ My)
Tsy9d19C10_fs08	1.0	$10^{19}$	10	prescribed velocity ( $t < 8$ My), free-slip ( $t > 8$ My)
Tsy9d19C30_fs08	1.0	$10^{19}$	30	prescribed velocity ( $t < 8$ My), free-slip ( $t > 8$ My)
Tsy9d21C01_v	1.0	$10^{21}$	1	prescribed velocity
Tsy9d21C10_v	1.0	$10^{21}$	10	prescribed velocity
Tsy9d21C30_v	1.0	$10^{21}$	30	prescribed velocity
Tsy9d21C01_fs08	1.0	$10^{21}$	1	prescribed velocity ( $t < 8$ My), free-slip ( $t > 8$ My)
Tsy9d21C10_fs08	1.0	$10^{21}$	10	prescribed velocity ( $t < 8$ My), free-slip ( $t > 8$ My)
Tsy9d21C30_fs08	1.0	$10^{21}$	30	prescribed velocity ( $t < 8$ My), free-slip ( $t > 8$ My)

own with the free-slip boundary condition from the initial state given in Fig. 1a without any additional push from the beginning.

First, let us discuss the plate behavior in the model with a lower stress limit ( $\sigma_y=0.1$  GPa), weaker decoupling layer ( $\eta_{\text{DL}}=10^{19}$  Pa·s), viscosity increase 10 at the 670 km boundary and a kinematic boundary condition at the surface (model Tsy8c19C10\_v).

Fig. 2 illustrates the time evolution of the slab in this model. The slab is descending relatively slowly at the beginning. When it passes the exothermic phase transition at 400 km, the plate velocity increases and reaches its maxima ( $\sim 20 \text{ cm}\cdot\text{yr}^{-1}$ , Fig. 3 red line). Then the plate velocity decreases when it arrives at the 670 km boundary. The subducting plate deforms above the phase transition at 670 km due to the mechanical resistance of the (more viscous) lower mantle and the endothermic phase transition. The deformation is facilitated by a rather low stress limit  $\sigma_y=0.1$  GPa. Then the deformed plate slowly penetrates into the lower mantle while the plate velocity slowly increases due to the increasing slab pull.

Though the surface velocity at the subducting plate is prescribed to be constant in this model case, the crust is relatively weak and thus subject to the significant deformation resulting in the velocity differentiation. This means that the horizontal velocity differs significantly between individual layers of the crust layer and plate and the slab velocity is only partly controlled by the surface boundary condition—to a certain extent it also reflects the negative buoyancy of the subducted part of the slab and the effect of the phase transitions. This is demonstrated in Fig. 3, where the horizontal velocity profile is shown in the Eulerian points, located at  $x=4800$  km and at the depths  $z=0, 5, 15, 25, 45, 65$  and 85 km. The blue line is for the point located at the top—it therefore obeys the boundary condition and keeps a constant velocity of  $5 \text{ cm}\cdot\text{yr}^{-1}$ . The green line is for the point located at the depth of 5 km that is within the weak crust. Here the velocity is already not fully controlled by the boundary condition and we observe the peak corresponding to the accelerating effect of the exothermic phase transition at a time of approximately 8 Myr.

The even deeper points (15–85 km) are already located within the stiff plate under the crust and their velocities are therefore identical (yellow–red line).

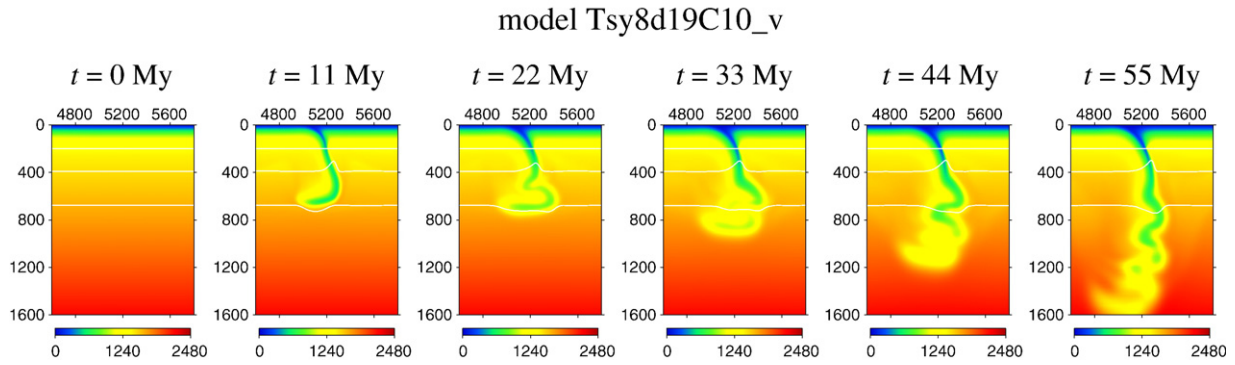


**Fig. 2.** Model Tsy8d19C10\_v: the time evolution of temperature [°C]. Part of the model domain (1600 km deep and 1200 km wide) is shown. White lines denote the depth 200 km and the phase transitions at 400 km and 670 km.

One time snapshot of this model is discussed in more detail in Fig. 4. We show here the temperature field  $T$  (panel a) and the temperature variation  $\Delta T$  with respect to the geotherm  $T_{\text{ref}}$  (panel b) to illustrate the slab morphology. The decadal logarithm of the relative viscosity and the prevailing deformation mechanisms are in panels c and d. By the prevailing deformation mechanism, we mean the mechanism which produces locally the lowest viscosity. The prevailing mechanism within the plate is mostly the stress limiter, especially in the upper mantle. In the vicinity of the plate, the dislocation creep prevails and in the rest of the mantle the diffusion creep dominates.

The velocity field is in Fig. 4 panel e. Note that the amplitude of the velocity is higher in the upper mantle than in the lower mantle, thus illustrating the buckling. The stress regime within the slab is demonstrated by the second invariant of the stress tensor (panel f) and by the decomposition of the stress tensor into the eigenvectors and eigenvalues (panel g). The axes are marked by lines and the values by a color field. The dilatation (panel g, blue color) is observed in the plate above the 400 km boundary due to the negative buoyancy effect of the exothermic phase transition. The dilatation can be observed also in the lower mantle in the outer part of the bent plate. The plate is compressed (red color) in the vertical direction between the depths of 400 km and 670 km due to the combined effect of both phase transitions and then in the lower mantle due to the viscous resistance of the lower mantle material.

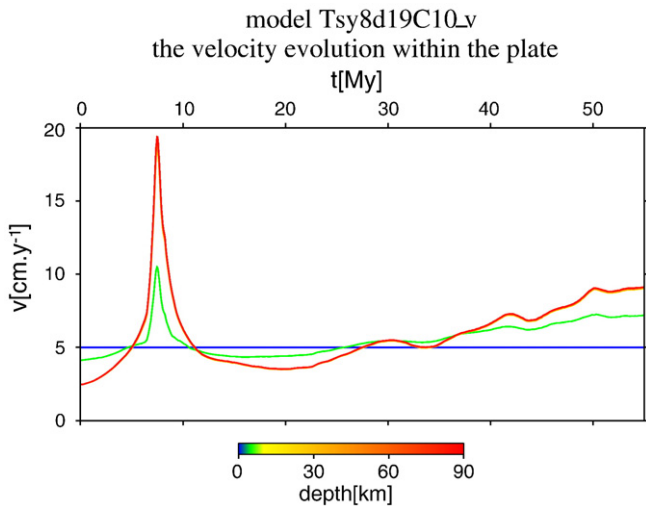


**Fig. 3.** Model Tsy8d19C10\_v: the time evolution of the velocity within the crust and plate. The profiles for eight Eulerian points located at  $x=4800$  km and depths  $z=0$  (blue), 5 (green) and 15, 25, 45, 65 and 85 km (yellow–red, the velocity is not differentiated). (For interpretation of the references to color in this figure legend, the reader is referred to the web version of this article.)

Until now, we have described the model Tsy8d19C10\_v with the phase transitions at 400 km and 670 km depths. Now, we try to isolate the effect of the phase transitions from the other factors influencing the slab morphology. To be able to study the influence of the phase transition, we subsequently switch on and off the individual phase transitions in the model Tsy8d19C10\_v. The results of this test are in Fig. 5; the snapshots were chosen when the plates reached approximately 1600 km depth. In panel a, there is an original model with both phase transitions. If both phase transitions are switched off (their Clapeyron slopes are set to zero), the buckling does not occur during the entire evolution of the slab (panel b). Only the tip of the subducting plate is slightly deformed due to the penetration to the more viscous lower mantle. If only the endothermic phase transition at the depth 670 km is considered, the buckling occurs only when the slab tip penetrates into the lower mantle (panel c). Later, as the slab pull increases, buckling does not occur any more. If only the exothermic phase transition at the depth 400 km is taken into account (panel d), significant buckling is observed (almost the same as in case of both phase transitions). Thus we can conclude that although both the exothermic and the endothermic phase transitions support the creation of the buckling instabilities, the effect of the 400 km phase transition has a more important effect on the slab thickening.

The results of all studied model cases are summarized in Fig. 6. We show here the temperature variations  $\Delta T$  with respect to the geotherm  $T_{\text{ref}}$ . The results for both lower stress limit (first and second rows) and higher stress limit (third and fourth rows) are given. The characteristics of the slabs (e.g. dip angle, thickening) depend on all tested parameters (stress limiter, surface boundary condition, viscosity increase in the lower mantle and the strength of the decoupling layer). All snapshots are taken approximately at the time when the slab reaches at the depth of  $\sim 1600$  km, except for the models q, r and x where the slab slowed down and the subduction process basically ceased.

Hence, the models at approximately same stage of the evolution are presented here. The slabs in the models with a lower stress limit (first two rows in Fig. 6) are easily deformed—they usually break, if there is no viscosity increase at 670 km depth (panels a and g–h), or often buckle if the viscosity increases in the lower mantle (panels c–f and k). For models with a higher stress limit (last two rows in Fig. 6), slabs in most models do not deform significantly, hardly any thickening occurs and bipolar structures of the stress tensor similar to the one reported by Čížková et al. (2007) are observed. The backward deflection develops in most models (panels m–r and u–v), especially if the crustal friction is low. The curvature of the slab arcs is higher in models with a weaker decoupling layer (panel m–n) than in models with higher viscosity crust (panel s–t). Some buckling is observed only for the model in panel w, where the relatively strong crust is able to transmit the effect of the prescribed surface velocity to the plate. Thus the plate is pushed to the mantle and some buckling

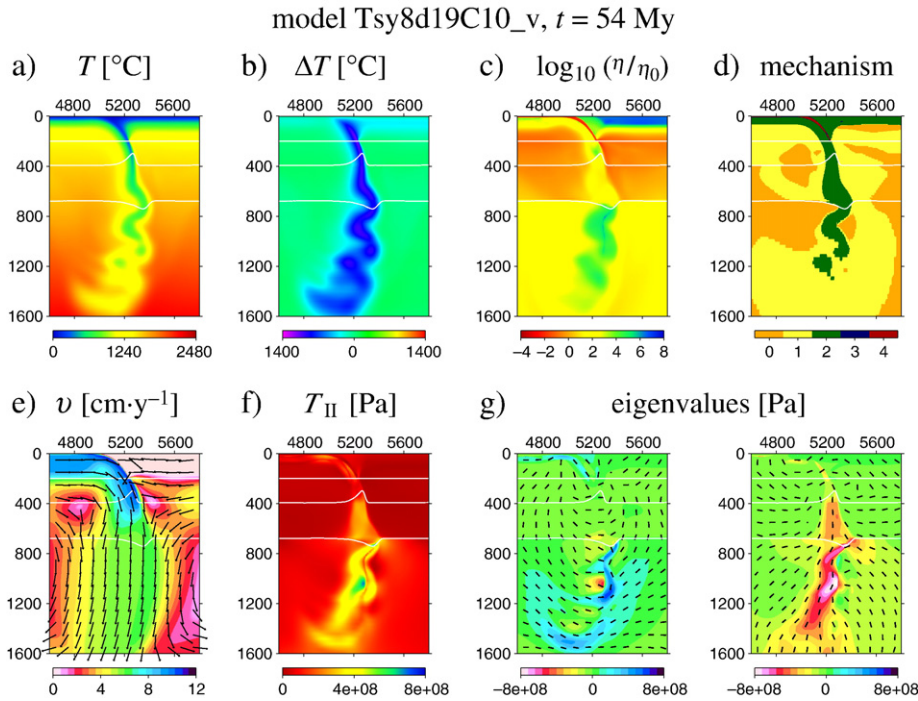


**Fig. 4.** Results for the model Tsy8d19C10\_v after 54 My, a) temperature  $T$ , b) temperature variation  $\Delta T$  with respect to geotherm  $T_{\text{ref}}$ , c) relative viscosity in the decadal logarithm scale  $\log_{10}(\eta/\eta_0)$ , d) prevailing deformation mechanism (0—diffusion creep, 1—dislocation creep, 2—stress limiter, 3—viscosity limit, 4—decoupling layer for  $z < 200$  km), e) velocity  $v$  (directions are marked by arrows, amplitudes by a color field), f) second invariant of the stress tensor  $\tau_{II}$  and g) stress tensor eigenvalues and eigenvectors (axes are marked by lines, amplitudes by a color field). Part of the model domain (1600 km deep and 1200 km wide) is shown. (For interpretation of the references to color in this figure legend, the reader is referred to the web version of this article.)

appears as the slab encounters the high viscosity lower mantle. The oscillations observed in some models with no viscosity jump, are the artefacts of insufficient resolution in these model cases and can be reduced by increasing the spatial resolution and decreasing the time step. Including the viscosity jump at the 670 km depth slows down the slab significantly (cf. the time of the snapshots in the individual columns of Fig. 6).

In the models with the lower stress limit and weak crust the slab buckling is observed in all models (c–f). Stronger coupling between the subducting and the over-riding plates (higher viscosity crust) tends against the buckling—if the viscosity contrast between the upper and the lower mantle is low ( $C = 10$ , i and j), one or two folds appear on the slab when it reaches the lower mantle, but then it

remains straight and relatively thin. If the higher value of the viscosity jump at 670 km ( $C = 30$ ) is considered, the buckling is observed only in the model run with the prescribed surface velocity (k). In a corresponding free-slip run (l) the plate thickens rather due to the compression and the conductive cooling. When the stiffer slabs (yield stress 1 GPa, last two rows of the Fig. 6) are considered, the viscosity jump at the 670 km depth by a factor of 10 has basically no effect on the plate thickness regardless of the crust viscosity (o–p and u–v). In the case of an even higher viscosity jump ( $C = 30$ ), the resistance of the viscous lower mantle is already quite strong and the plate can only penetrate if an additional push provided by the kinematic surface boundary condition adds to a slab pull (w). In the free-slip runs (r and x), the stiff slab with high internal resistance against the bending

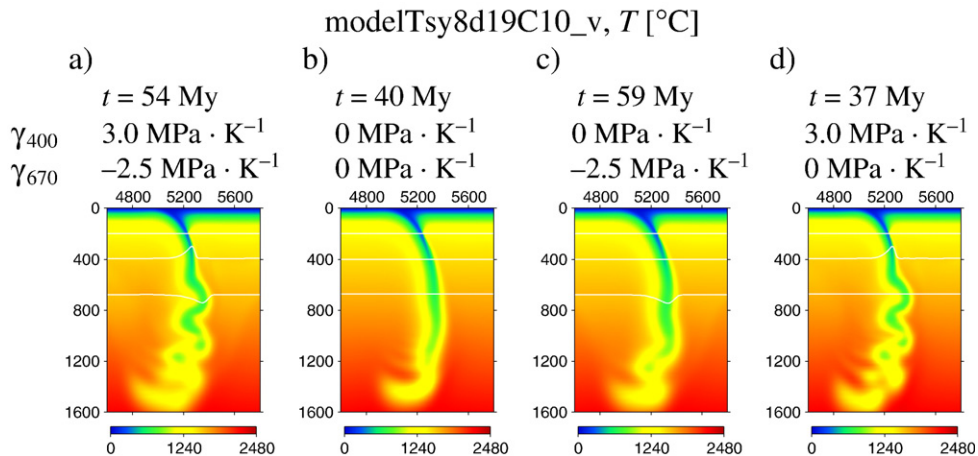


**Fig. 5.** The effect of the individual phase transitions. Results for the model Tsy8d19C10\_v with a) both phase transitions at the depths 400 km and 670 km, b) no phase transitions, c) one phase transition at 670 km depth and d) one phase transition at 400 km depth. Part of the model domain (1600 km deep and 1200 km wide) is shown.

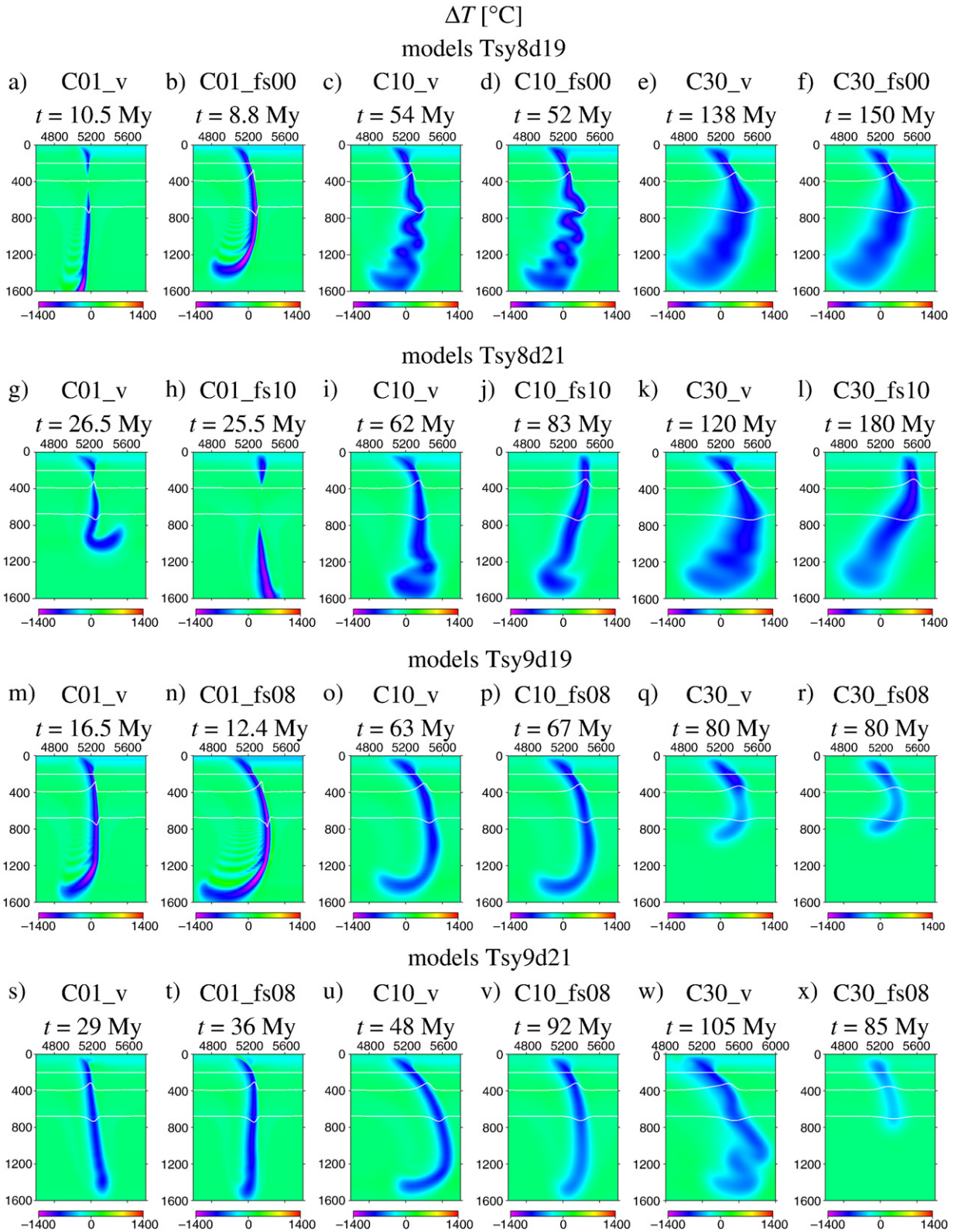


**Fig. 6.** Summary of the results for all models. The temperature variations  $\Delta T$  [°C] with respect to the geotherm  $T_{\text{ref}}$  are shown in 1600 km deep and 1200 km wide part of the model domain.

slows down when it encounters the mechanical barrier of the highly viscous lower mantle and the subduction process basically stops. The same is true for the model with a prescribed surface velocity but with a low viscosity decoupling crust (q). Here the weak decoupling layer is not able to transmit the push of the surface boundary condition to the

plate and the model results are very similar to the corresponding free-slip run (cf. r). Generally we can state that no thickening or buckling occurs if either no viscosity increase at 670 km depth is prescribed (first two columns), or if a higher stress limit is used regardless of the viscosity jump at 670 km (third and fourth rows except panel w).

Thick slabs are observed only in the models with a lower stress limit (0.1 GPa) with viscosity increase at 670 km. They are formed by buckling (c–f) and/or by compression and conductive cooling (panel l).

### 3.1. Seismic velocity anomalies

Finally, let us try to compare the results of our numerical modeling with seismic tomography. For this purpose, we need to convert our temperature anomalies to seismic velocity ones. The seismic velocity anomalies can be calculated from the thermal and compositional structure of the mantle using the appropriate partial derivatives (sensitivities)—e.g. [Deschamps and Trampert \(2003\)](#). The seismic velocities and their derivatives depend on the elastic properties and the equation of state of the mantle minerals. To obtain the elastic parameters of the lower mantle material, we use the code kindly provided by Renata M. Wentzcovitch. It calculates polycrystalline multiphase averages of the bulk and shear moduli using an arithmetic averages scheme. We employ the mineralogical model by [Ringwood \(1975\)](#) including perovskite (Pv)  $(\text{Mg}_{1-x}\text{Fe}_x)\text{SiO}_3$  and magnesiowüstite (Mw)  $(\text{Mg}_{1-y}\text{Fe}_y)\text{O}$ . We take the same percentage of iron for both these minerals, i.e.  $x=y=0.12$ . Further, we have to specify the ratio of magnesiowüstite to perovskite. We define it using Mw the volume fraction of magnesiowüstite  $v_f = \frac{V^{\text{Mw}}}{V^{\text{Mw}}+V^{\text{Pv}}} = 0.2$  at 30 GPa and 2000 K. For computing the polycrystalline average of the elastic properties, we use the formulas

$$\begin{aligned} K_s(p, T) &= v_f K_s^{\text{Mw}}(p, T) + (1 - v_f) K_s^{\text{Pv}}(p, T), \\ G(p, T) &= v_f G^{\text{Mw}}(p, T) + (1 - v_f) G^{\text{Pv}}(p, T), \end{aligned} \quad (12)$$

where  $K_s$  and  $G$  are the bulk and the shear moduli, respectively. Our calculations are based on the elastic properties and equation of

state of perovskite  $\text{MgSiO}_3$  by [Karki et al. \(2000b\)](#) and [Wentzcovitch et al. \(2004\)](#). The elastic properties and equation of state of magnesiowüstite are in [Karki et al. \(1999\)](#) and [Karki et al. \(2000a\)](#). For including the iron content, we use corrections by [Kiefer et al. \(1999\)](#) and [Karki et al. \(1999\)](#) for  $(\text{Mg}_{1-x}\text{Fe}_x)\text{SiO}_3$  and  $(\text{Mg}_{1-y}\text{Fe}_y)\text{O}$ , respectively. Once we have the moduli  $K_s$  and  $G$ , P-wave velocities are calculated as

$$v_p(p, T) = \sqrt{\frac{K_s(p, T) + \frac{4}{3}G(p, T)}{\rho(p, T)}} \quad (13)$$

Then we calculate the derivatives  $\frac{\partial v_p}{\partial T}(p, T)$  numerically.

We compute the seismic velocity anomalies for our subduction models as follows:

$$\frac{\delta v_p}{v_p}(p(z), T(x, z)) = \frac{\partial v_p}{\partial T}(p(z), T(x, z)) \cdot \Delta T(x, z) \frac{1}{v_p(p(z), T_{\text{ref}}(z))}. \quad (14)$$

For several models where the slab thickening occurs ([Fig. 6](#), panels c–f, k, l and w), the P-wave velocity anomalies are given in [Fig. 7](#). Similarly to [Ribe et al. \(2007\)](#), we show here the isolines of seismic velocity anomaly for 0.2% and 0.3%. The estimated slab widths are given in [Fig. 7](#). We obtain comparable slab widths for models with a lower stress limit, weaker decoupling layer and viscosity jump 10 ([Fig. 7](#), models a–b). In these cases, the slab widths are approximately 360 km below the 670 km boundary. For models with the viscosity increase 30 at 670 km and lower stress limit ([Fig. 7c–f](#)), the slab velocity in the lower mantle is low (up to  $\sim 2 \text{ cm} \cdot \text{yr}^{-1}$ ) and conductive cooling of the ambient mantle is rather efficient; therefore the plates become considerably wider than in the previous case. For these models, the slabs widths are in the range (580–800 km) below the

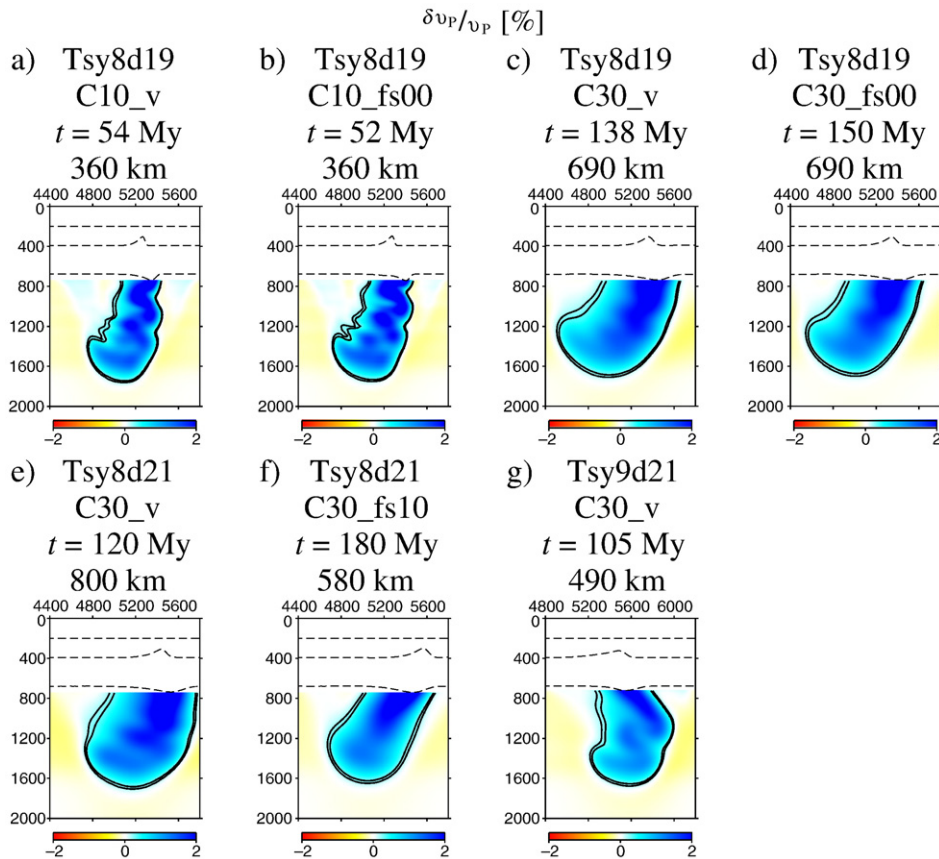


**Fig. 7.** The estimated minimal width of the slabs below 670 km for some of the models. We show the seismic velocity anomalies in the lower mantle. The isolines  $\delta v_p/v_p=0.2$  and 0.3% are marked by the solid lines. Dashed lines denote the depth 200 km and the phase transitions at 400 km and 670 km depths. Part of the model domain (2000 km deep and 1600 km wide) is shown.

670 km boundary (Fig. 7c–f). For the only model with a higher stress limit which shows lower mantle thickening, the estimated width below the 670 km boundary is 490 km.

#### 4. Discussion and conclusions

We investigated here the effect of several parameters (the yield stress, the viscosity of the crust, the viscosity jump at the 670 km boundary) and of the surface boundary conditions (prescribed velocity vs. free-slip) on the formation of the thick, blob-like structures in the upper part of the lower mantle.

The thickening of the slabs in the lower mantle is caused by two mechanisms—buckling and/or thickening due to the compression. Among the studied parameters, the yield stress and the viscosity of the crust were found to be the most important factors controlling the thickness of the lower mantle cold anomalies. We therefore fix the other parameters (viscosity jump at 670 km is 10 and only the kinematic surface boundary condition was applied) and look more closely at the effect of the main controlling parameters. If we take the maximum width of the seismically fast structures in the lower mantle (defined by the 0.2–0.3% isoline, similarly to Fig. 7) and the number of buckles (folds) as the two parameters which characterize the lower mantle slabs, we can roughly divide our parameter space into three regions (Fig. 8). If the yield stress is high ( $\sigma_y > 0.3$  GPa) neither buckling nor compressive thickening occurs in our models (region I in Fig. 8) and the slabs have more or less constant width throughout the lower mantle. If the yield stress is lower, we observe two regimes of thickening. In case of relatively weak decoupling crustal layer ( $\eta_{DL} < 2 \cdot 10^{20}$  Pa·s), we have thick buckled slabs (region II in Fig. 8). The slabs with stronger coupling between the subducting and over-riding plates (higher crustal viscosity) do not buckle (except for one or two folds at the moment when they arrive at the 670 km depth), but thicken due to the compression (region III in Fig. 8).

Our analysis was performed for relatively old slabs ( $t = 100$  My). For the younger slabs, smaller resistance against the bending could be expected (their temperature is higher and their thickness is smaller), therefore the formation of buckled anomalies should be easier (Enns et al., 2005). Further, we used the activation parameters based on the experimentally derived values (Frost and Ashby, 1982; Karato and Wu, 1993; Yamazaki and Karato, 2001). The yield stress of the power-law stress-limiting mechanism is much less constrained. Peierl's creep suggests the value of about 1 GPa (Kameyama et al., 1999). In the modelling studies the values in the range 0.1 GPa to 1 GPa are often

assumed (van Hunen et al., 2004; Čížková et al., 2007). Our results prefer the lower values of the yield stress—if the values of about 1 GPa are used, the slabs are too stiff to be deformed. This is in agreement with e.g. the results of (Čížková et al., 2002) who conclude that if the stress limit of 1 GPa is applied, the slabs in the transition zone are too strong to be deformed and an extra weakening mechanism is needed (e.g. the grain size weakening of the diffusion creep viscosity). The viscosity has to increase at the 670 km boundary in order to find any thickening of the slabs. We assumed here the maximum viscosity increases by a factor  $C = 30$ , even though some authors argue for a much higher increase—up to 100–1000 (Forte and Mitrovica, 1996; Kido and Čadež, 1997). In our model setup it would be, however, difficult to have the slab penetrating into the lower mantle, if a yet higher viscosity jump would be prescribed. Already in the model with the viscosity increase by a factor 30, the subduction process is nearly stopped in the models with free-slip, where the subduction process is driven only by the slab pull. The same is true in the models with a prescribed surface velocity and a low viscosity crust, which is not able to transmit the push of the boundary condition to the slab. This extra push provided by the surface boundary condition is necessary to maintain the subduction process and force the slab to penetrate into the highly viscous lower mantle.

The formation of the buckling instabilities in our models is in good agreement with previous works. E.g. Christensen (1996) used a 2D Cartesian model of subduction with depth- and temperature dependent viscosity and obtained buckling features for models with a viscosity jump at 660 km or with a strong phase transition at 660 km. Houseman and Gubbins (1997) also obtained the buckling in the simulations of the slab deformation in the model with non-linear (strain-rate dependent) viscosity. In the model with a composite rheology, McNamara et al. (2001) found buckling instabilities, whose degree increased with decreasing plate strength. In a 2D Cartesian model with visco-plastic rheology but without phase transitions, Enns et al. (2005) also predict buckling—a higher degree of buckling is observed for weak and thin plates.

In some models with the free-slip, lower stress limiter and stronger decoupling layer we observe the forward shift of the trench (models in Fig. 6 panel h, j and l). The trench migrates to the right, i.e. in the direction of the subducting plate. In these models the coupling between the crustal layer and the subducting and the over-riding plates is rather strong and as a consequence of the relatively low stress limit, the over-riding plate can deform and a part of it may subduct together with the subducting plate.

Some of our models with the weaker decoupling layer (models b, m and n in Fig. 6) produce rather high plate velocities—up to  $\sim 75$  cm·yr<sup>-1</sup> depending on the viscosity increase at 670 km. There are several possible explanations for such high velocities not observed in nature. It is possible that this particular model underestimates the friction at the contact between the subducting and the over-riding plates and/or the viscosity in the lower mantle. The high velocities could also be attributed to the 2D limitations of the model—in a 3D reality the depth of the slab tip is not uniform along the whole subduction line and the plate does not reach the phase transition depth at 400 km instantaneously along the line and the speeding effect of an exothermic phase transition could be lower. Another candidate to slow down extremely fast subduction is the effect of metastable olivine, whose buoyancy increases when penetrating into the lower mantle (Tetzlaff and Schmeling, 2000). Further, the non-linear behavior of the crustal rheology may be important for suppressing the high plate velocities. Especially, the effect of the water presence within the oceanic crust should play an important role (e.g. Gerya et al., 2006, 2008).

The water content may depend on the plate velocity—the amount of water within the crust is suggested to increase with the decreasing plate velocity (Gorczyk et al., 2007). Consequently, the viscosity of the crust increases with increasing plate velocity—such an effect is

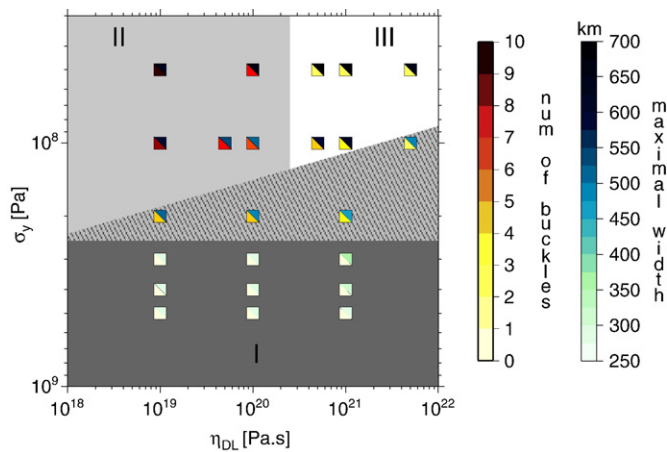


**Fig. 8.** The thickening of the slabs in the models with a viscosity increase  $C = 10$  and a prescribed velocity at the surface. The maximal width and the number of buckles are shown as a function of the crustal viscosity  $\eta_{DL}$  and the yield stress  $\sigma_y$ . The parameter space can be divided into three regimes—I (region with no buckling or thickening), II (region with thickening due to the buckling) and III (region with thickening mainly due to the compression). The hatched area marks the transition between the regimes.

therefore opposite to the effect of the increasing stress in the dislocation creep.

The resulting shape and the wavelength of the subducting plate in the lower mantle depends strongly on the coupling between the plates, i.e. on the strength of the crust. In the oceanic plates, the crust consists of less-dense basalt. As it subducts, it transforms into stronger and denser eclogite by a series of phase transitions. The properties of the basalt-to-eclogite metamorphism and the rheological properties of basalt and eclogite are not well known and they strongly depend on the content of water and fugacity (Kohlstedt et al., 1995).

Vlaar et al. (1994) use dislocation creep of diabase to describe rheological properties of both basalt and eclogite. For temperature intervals of 600 °C and 1750 °C, they get viscosities between  $\sim 10^{19}$ – $10^{21}$  Pa·s for  $\dot{\epsilon}_{II} = 10^{-15}$  s<sup>-1</sup>.

Here we use a simple approximation of the crustal properties—crust material has no density contrast with respect to the mantle material and we assume two constant values of its viscosity ( $10^{19}$  Pa·s and  $10^{21}$  Pa·s) in agreement with the above mentioned results by Vlaar et al. (1994). The effect of the crustal layer parametrization should be subject to a more detailed study in future.

We found that the results of the seismic tomography suggesting the existence of the blob-like structures in the lower mantle can be explained by the thickening or buckling of the subducting slabs. Based on our assumptions and under the model limitations, we conclude that our model requires rather a low yield stress of the stress-limiting mechanism ( $\lesssim 0.3$  GPa) and prefers the lower viscosity of the crust ( $\eta_{DL} \lesssim 10^{20}$  Pa·s) in order to obtain the cold structures in agreement with the tomographic images of the lower mantle. Besides the viscosity increase by a factor 10–30 at the depth of 670 km, the presence of the major upper mantle phase transitions, especially the exothermic one at 400 km depth, are necessary to create the buckling instabilities.

## Acknowledgments

We thank Renata Wentzcovitch for providing the code for calculating the elastic moduli and Dave Yuen for inviting M.B. to the MSI—part of this work was done during this visit. We thank Ondřej Čadek and Radek Matyska for fruitful discussions. Our gratitude also belongs to Alistair Bargery for English corrections. The comments of Neil Ribe, Harro Schmeling and Rob van der Hilst that helped to improve the manuscript significantly are gratefully acknowledged. This work was supported by the Research Program MSM0021620860 of the Ministry of Education, by Charles University Grant Agency (GAUK 133307) and by MCRTN project "c2c the fate of subducted material".

## References

Běhounková, M., 2007. Global and regional scale modeling of dynamic processes in the Earth's mantle, Ph.D. thesis, Charles University in Prague. URL [http://www.geo.mff.cuni.cz/~behounek/papers/Behounkova\\_phd.pdf](http://www.geo.mff.cuni.cz/~behounek/papers/Behounkova_phd.pdf).

Bijwaard, H., Spakman, W., Engdahl, E.R., 1998. Closing the gap between regional and global travel time tomography. *J. Geophys. Res.* 103, 30055–30075.

Bina, C., Helffrich, G., 1994. Phase transition Clapeyron slopes and transition zone seismic discontinuity topography. *J. Geophys. Res.* 103, 15853–15860.

Boyd, T., Creager, K., 1991. The geometry of Aleutian subduction: three-dimensional seismic imaging. *J. Geophys. Res.* 96, 2267–2291.

Bunge, H.P., Richards, M.A., Baumgardner, J.R., 1996. Effect of depth-dependent viscosity on the planform of mantle convection. *Nature* 379, 436–438.

Christensen, U.R., 1996. The influence of trench migration on slab penetration into the lower mantle. *Earth Planet. Sci. Lett.* 140, 27–39.

Christensen, U.R., Yuen, D.A., 1984. The interaction of a subducting lithospheric slab with a chemical or phase boundary. *J. Geophys. Res.* 89, 4389–4402.

Christensen, U.R., Yuen, D.A., 1985. Layered convection induced by phase transitions. *J. Geophys. Res.* 90, 10291–10300.

Čížková, H., Čadek, O., 1997. Effect of a viscosity interface at 1000 km depth on mantle convection. *Stud. Geophys. Geod.* 41, 297–306.

Čížková, H., van Hunen, J., van den Berg, A.P., Vlaar, N.J., 2002. The influence of rheological weakening and yield stress on the interaction of slabs with 670 km discontinuity. *Phys. Earth Planet. Inter.* 199, 447–457.

Čížková, H., van Hunen, J., van den Berg, A.P., 2007. Stress distribution within subducting slabs and their deformation in the transition zone. *Phys. Earth Planet. Inter.* 161, 202–214. doi:10.1016/j.pepi.2007.02.002.

Creager, K., Jordan, T., 1986. Slab penetration into the lower mantle beneath the Mariana and other island arcs of the northwest Pacific. *J. Geophys. Res.* 91, 3573–3589.

Deschamps, F., Trampert, J., 2003. Mantle tomography and its relation to temperature and composition. *Phys. Earth Planet. Inter.* 140, 277–291.

Enns, A., Becker, T.W., Schmeling, H., 2005. The dynamics of subduction and trench migration for viscosity stratification. *Geophys. J. Int.* 160, 761–775.

Fischer, K., Jordan, T., 1991. Seismic strain rate and deep slab deformation in Tonga. *J. Geophys. Res.* 96, 14429–14444.

Forté, A.M., Mitrovica, J.X., 1996. New inferences of mantle viscosity from joint inversion of long-wavelength mantle convection and post-glacial rebound data. *Geophys. Res. Lett.* 23, 1147–1150.

Frost, H.J., Ashby, M.F., 1982. *Deformation Mechanism Maps*. Pergamon Press, Oxford.

Fukao, Y., To, A., Obayashi, M., 2003. Whole mantle P wave tomography using P and PP-P data. *J. Geophys. Res.* 108 (2021).

Gaherty, J.B., Hager, B.H., 1994. Compositional vs. thermal buoyancy and the evolution of subducted lithosphere. *Geophys. Res. Lett.* 21, 141–144.

Gerya, T.V., Yuen, D.A., 2003. Characteristics-based marker-in-cell method with conservative finite-differences schemes for modeling geological flows with strongly variable transport properties. *Phys. Earth Planet. Inter.* 140, 293–318.

Gerya, T.V., Perchuk, L.L., van Reenen, D.D., Smit, C.A., 2000. Two-dimensional numerical modeling of pressure–temperature–time paths for the exhumation of some granulite facies terrains in the precambrian. *J. Geodyn.* 30, 17–35.

Gerya, T.V., Connolly, J.A.D., Yuen, D.A., Górczyk, W., Capel, A.M., 2006. Seismic implications of mantle wedge plumes. *Phys. Earth Planet. Inter.* 156, 59–74.

Gerya, T.V., Connolly, J.A.D., Yuen, D.A., 2008. Why is terrestrial subduction one-sided? *Geology* 36, 43–46.

Giardini, D., Woodhouse, J., 1984. Deep seismicity and modes of deformation in Tonga subduction zone. *Nature* 307, 551–555.

Górczyk, W., Willner, A.P., Gerya, T.V., Connolly, A.D.J., Burg, J.P., 2007. Physical controls of magmatic productivity at Pacific-type convergent margins: numerical modelling. *Phys. Earth Planet. Inter.* 163, 209–232.

Griffiths, R., Hackney, R., van der Hilst, R., 1995. A laboratory investigation of effects of trench migration on the descent of subducted slabs. *Earth Planet. Sci. Lett.* 133 (17), 1–17.

Griffiths, R.W., Turner, J.S., 1988. Viscous entrainment by sinking plumes. *Earth Planet. Sci. Lett.* 90, 467–477.

Guillou-Frottier, L., Buttles, J., Olson, P., 1995. Laboratory experiments on the structure of subducted lithosphere. *Earth Planet. Sci. Lett.* 133 (16), 19–34.

Gurnis, M., Hager, B.H., 1988. Controls of the structure of subducted slabs. *Nature* 335, 317–321.

Hager, B.H., Richards, M.A., 1989. Long wavelength variation in Earth's geoid: physical models and dynamical implications. *Philos. Trans. R. Soc. Lond.* 328, 309–327.

Hockney, R.W., Eastwood, J.W., 1988. *Computer Simulations Using Particles*. IOP Publishing Ltd, Bristol.

Houseman, G.A., Gubbins, D., 1997. Deformation of subducted oceanic lithosphere. *Geophys. J. Int.* 131, 535–551.

Inoue, H., Fukao, Y., Tanabe, T., Ogata, Y., 1990. Whole mantle P-wave travel time tomography. *Phys. Earth Planet. Inter.* 59, 294–328.

Ita, J., King, S.D., 1994. Sensitivity of convection with an endothermic phase change to the form of governing equations, initial conditions, boundary conditions, and equation of state. *J. Geophys. Res.* 99, 15919–15938.

Kameyama, M., Yuen, D.A., Karato, S.I., 1999. Thermal-mechanical effects of low-temperature plasticity (the Peierls mechanism) on the deformation of viscoelastic shear zone. *Earth Planet. Sci. Lett.* 168, 159–172.

Káráson, H., van der Hilst, R.D., 2001. Tomographic imaging of the lowermost mantle with differential times of refracted and diffracted core phases (PKP, PKPdiff). *J. Geophys. Res.* 106, 6569–6587.

Karato, S.I., Wu, P., 1993. Rheology of the upper mantle: a synthesis. *Science* 260, 83–108.

Karki, B.B., Wentzcovitch, R.M., de Gironcoli, S., Baroni, S., 1999. First-principles determination of elastic anisotropy and wave velocities of MgO at lower mantle conditions. *Science* 286, 1705–1707.

Karki, B.B., Wentzcovitch, R.M., de Gironcoli, S., Baroni, S., 2000a. High-pressure lattice dynamics and thermoelasticity of MgO. *Phys. Rev. B* 61, 8793–8800.

Karki, B.B., Wentzcovitch, R.M., de Gironcoli, S., Baroni, S., 2000b. Ab initio lattice dynamics of MgSiO<sub>3</sub> perovskite at high pressure. *Phys. Rev. B* 62, 14,750–14,756.

Kido, M., Čadek, O., 1997. Inferences of viscosity from the oceanic geoid: indication of a low viscosity zone below the 660-km discontinuity. *Earth Planet. Sci. Lett.* 151, 125–137.

Kiefer, B., Stixrude, L., Wentzcovitch, R.M., 1999. Elasticity of (Mg,Fe)SiO<sub>3</sub>-perovskite at high pressures. *Geophys. Res. Lett.* 29 (11), 1539.

Kohlstedt, D.L., Evans, B., Mackwell, S.J., 1995. Strength of the lithosphere: constraints imposed by laboratory experiments. *J. Geophys. Res.* 100, 17,587–17,602.

Lambeck, K., Johnston, P., 1998. The viscosity of the mantle: evidence from analysis of glacial-rebound phenomena. In: Jackson, I. (Ed.), *The Earth's Mantle: Composition, Structure and Evolution*. Cambridge University Press, pp. 461–502.

McNamara, A.K., Karato, S.I., van Keken, P.E., 2001. Localization of dislocation creep in the lower mantle: implications for the origin of seismic anisotropy. *Earth Planet. Sci. Lett.* 191, 85–99.

Peltier, W.R., 1996. Mantle viscosity and ice-age ice sheet tomography. *Science* 273 (5280), 1359–1364.

Ren, Y., Stutzmann, E., van der Hilst, R.D., Besse, J., 2007. Understanding seismic heterogeneities in the lower mantle beneath the Americas from seismic

- tomography and plate tectonic history. *J. Geophys. Res.* 112, b01302. doi:10.1029/2005JB004154.
- Ribe, N.M., 2003. Periodic buckling of viscous sheets. *Phys. Rev. E* 68 (036305).
- Ribe, N.M., Stutzmann, E., Ren, Y., van der Hilst, R.D., 2007. Buckling instabilities of subducted lithosphere beneath the transition zone. *Earth Planet. Sci. Lett.* 254, 173–179.
- Ricard, Y., Richards, M., Lithgow-Bertelloni, C., le Stunff, Y., 1993. A geodynamic model of mantle density heterogeneity. *J. Geophys. Res.* 98, 21,895–21,909.
- Richards, M., Ricard, Y., Lithgow-Bertelloni, C., Spada, G., Sabadini, R., 1997. An explanation for Earth's long term rotational stability. *Science* 275, 372–375.
- Ringwood, A.E., 1975. *Composition and Petrology of the Earth's Mantle*. McGraw-Hill, New York.
- Steinbach, V., Yuen, D.A., 1995. The effects of temperature dependent viscosity on mantle convection with two mantle major phase transitions. *Phys. Earth Planet. Inter.* 90, 13–36.
- Su, W.J., Woodward, R.L., Dziewonski, A.M., 1994. Degree-12 model of shear velocity heterogeneity in the mantle. *J. Geophys. Res.* 99, 4945–4980.
- Tackley, P.J., Stevenson, D.J., Glatzmaier, G.A., Schubert, G., 1993. Effects of an endothermic phase transition at 670 km depth in a spherical model of convection in the Earth's mantle. *Nature* 361, 699–704.
- Tetzlaff, M., Schmeling, H., 2000. The influence of olivine metastability on deep subduction of oceanic lithosphere. *Phys. Earth Planet. Inter.* 120, 29–38.
- van den Berg, A.P., van Keken, P.E., Yuen, D.A., 1993. The effects of a composite non-Newtonian and Newtonian rheology on mantle convection. *Geophys. J. Int.* 115, 62–78.
- van der Hilst, R.D., 1995. Complex morphology of subducted lithosphere in the mantle beneath the Tonga trench. *Nature* 374, 154–157.
- van der Hilst, R.D., Widiyantoro, S., Engdahl, E.R., 1997. Evidence for deep mantle circulation from global tomography. *Nature* 386, 578–584.
- van Hunen, J., 2001. Shallow and buoyant lithospheric subduction: causes and implications from thermo-chemical numerical modeling, Ph.D. thesis, Utrecht University.
- van Hunen, J., van den Berg, A.P., Vlaar, N.J., 2004. Various mechanisms to induce present-day shallow flat subduction and implications for the younger Earth: a numerical parameter study. *Phys. Earth Planet. Inter.* 146, 179–194.
- Vasco, D.W., Johnson, L.R., Pulliam, R.J., 1995. Lateral variation in mantle velocity structure and discontinuities determined from P, PP, S, SS and SS-SdS travel time residuals. *J. Geophys. Res.* 100, 24037–24059.
- Vasco, D.W., Johnson, L.R., Marques, O., 2003. Resolution, uncertainty, and whole Earth tomography. *J. Geophys. Res.* 108 (2022).
- Vlaar, N.J., van Keken, P.E., van den Berg, A.P., 1994. Cooling of the Earth in the Archaean: consequences of pressure-release melting in a hotter mantle. *Earth Plan. Sci. Lett.* 121, 1–18.
- Wentzcovitch, R.M., Karki, B.B., Cococcioni, M., de Gironcoli, S., 2004. Thermoelastic properties of MgSiO<sub>3</sub>-perovskite: insights on the nature of the Earth's lower mantle. *Phys. Rev. Lett.* 92 (018501).
- Yamazaki, D., Karato, S.I., 2001. Some mineral physics constraints on the rheology and geothermal structure of Earth's lower mantle. *Am. Mineral.* 86, 385–391.